

# RN-SDEs: Limited-Angle CT Reconstruction with Residual Null-Space Diffusion Stochastic Differential Equations

Jiaqi Guo, Santiago Lopez-Tapia, Wing Shun Li, Yunnan Wu, Marcelo Carignano, Vadim Backman, Vinayak P. Dravid, and Aggelos K. Katsaggelos

**Abstract**—Computed tomography is a widely used imaging modality with applications ranging from medical imaging to material analysis. One major challenge arises from the lack of scanning information at certain angles, leading to distorted CT images with artifacts. This results in an ill-posed problem known as the Limited Angle Computed Tomography (LACT) reconstruction problem. To address this problem, we propose Residual Null-Space Diffusion Stochastic Differential Equations (RN-SDEs), which are a variant of diffusion models that characterize the diffusion process with mean-reverting (MR) stochastic differential equations. To demonstrate the generalizability of RN-SDEs, our experiments are conducted on two different LACT datasets, i.e., ChromSTEM and C4KC-KiTS. Through extensive experiments, we show that by leveraging learned Mean-Reverting SDEs as a prior and emphasizing data consistency using Range-Null Space Decomposition (RNSD) based rectification, RN-SDEs can restore high-quality images from severe degradation and achieve state-of-the-art performance in most LACT tasks. Additionally, we present a quantitative comparison of computational complexity and runtime efficiency, highlighting the superior effectiveness of our proposed approach.<sup>1</sup>

**Index Terms**—Limited-angle CT reconstruction, Diffusion stochastic differential equations, Mean-reverting diffusion, Range-null space decomposition

## I. INTRODUCTION

Computed Tomography (CT) is a widely used imaging modality employed in various fields, including diagnostic medical imaging, industrial non-destructive testing, and materials analysis [1]–[4]. The fundamental working principle of CT involves the transmission of a series of parallel X-ray beams through the object from different angles. This process can be mathematically represented by the Radon Transform [5], in which a series of line integrals are calculated for each projection angle, representing the cumulative X-ray absorption along certain scanning trajectories. Ideally, projections obtained from a full range of projection angles would contain the entire Fourier domain information of the observed object, allowing a direct and precise reconstruction. However, in more common situations, constraints in experimental setups can hinder uniform projection sampling, restricting information

to limited angles. This issue poses a challenge to conventional reconstruction methods such as Filtered Back Projection (FBP) [6] and is referred to as the **Limited Angle Computed Tomography (LACT)** problem. The central slice theory [7] states that a single one-dimensional projection at an angle corresponds to a line through the two-dimensional Fourier space. We show this relationship in Fig. 1 and denote the missing angles as  $\theta_{miss}$ .

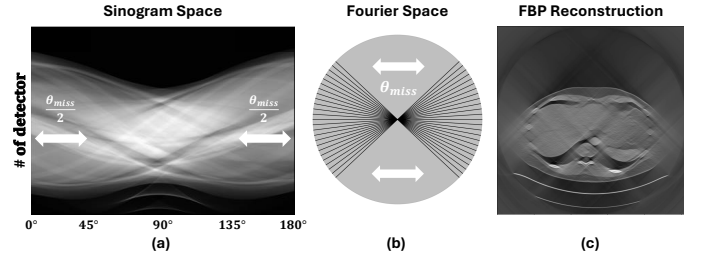


Fig. 1. Illustration of limited angle tomography, with missing angle,  $\theta_{miss}$ , set to be  $90^\circ$ . (a) Sinogram of an exemplary 2D observation with certain angles missing; (b) Sampling process in the Fourier space; (c) Reconstruction using the FBP algorithm, with distortion and artifacts presents

**Image Restoration for LACT:** Image restoration (IR) is the problem of estimating a high-quality (HQ) image  $\mathbf{x}$  from a low-quality (LQ) observed measurement  $\mathbf{y}$ . Usually, the degraded image  $\mathbf{y}$  can be simply expressed by a linear model as:

$$\mathbf{y} = \mathbf{A}\mathbf{x} + \mathbf{n} \quad (1)$$

where  $\mathbf{n}$  is typically additive white Gaussian noise and  $\mathbf{A}$  is a known linear operation. Particularly, in the context of LACT,  $\mathbf{A}$  denotes the Radon transform that defines a mapping from a three-dimensional object in a vector form,  $\mathbf{x} \in \mathbb{R}^M$  to a set of projections,  $\mathbf{y} \in \mathbb{R}^N$ . Those projections are commonly referred to as a sinogram, a term that describes the unique pattern formed by the Radon transform of an object, resembling a series of sine waves. A typical solution to this problem is to employ a model-based optimization process, whose solution can be formulated as:

$$\hat{\mathbf{x}} = \arg \min_{\mathbf{x}} \frac{1}{2\sigma^2} \|\mathbf{A}\mathbf{x} - \mathbf{y}\|_2^2 + \lambda \mathcal{R}(\mathbf{x}). \quad (2)$$

The fidelity term  $\frac{1}{2\sigma^2} \|\mathbf{A}\mathbf{x} - \mathbf{y}\|_2^2$  ensures the consistency between the estimation and observation, whereas the subsequent image-prior term,  $\lambda \mathcal{R}(\mathbf{x})$ , imposes constraints on the estimation using formulaic prior knowledge, e.g., Tikhonov

Jiaqi Guo, Santiago Lopez-Tapia, Yunnan Wu, and Aggelos K. Katsaggelos are with the Department of Electrical and Computer Engineering, Northwestern University, IL 60201 USA (e-mail: jiaqi.guo@northwestern.edu; a-katsaggelos@northwestern.edu)

Wing Shun Li and Vinayak P. Dravid are with the Applied Physics Program, Northwestern University, Evanston, IL 60201 USA

<sup>1</sup>The code is available at <https://github.com/GuoJiaqi-1020/RN-SDE>

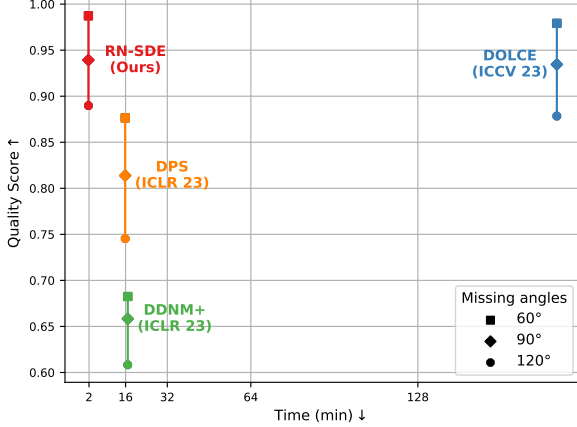


Fig. 2. Quantitative performance evaluation on C4KC-KiTS dataset [26]. This plot demonstrates the relationship between the image quality and average processing time per slide in terms of minutes. The quality is measured as the average of the value of the relative performance of each method in each of three metrics (PSNR, SSIM, and LPIPS [27]) with respect to the highest value obtained by the best method on that metric, respectively. Our proposed RN-SDE obtains, on average, higher quality while having significantly lower computational complexity. More details are provided in Section IV-D.

regularization, total variation distance, transform-domain sparsity and dictionary learning [8]–[11].

The evolution of deep learning (DL) has introduced a new pattern of solving LACT tasks. One straightforward approach is to train a convolutional neural network (CNN),  $\mathcal{Z}_\theta$ , with learnable parameters  $\theta$ , to directly perform a regularized inversion of the Radon transform [12]–[17]. Typically, they seek to minimize the mean squared error (MMSE) between the restored image  $\mathcal{Z}_\theta(\mathbf{y})$ , and the GT images  $\mathbf{x}$ . Those MMSE-based methods circumvent the explicit modeling  $\mathbf{A}$  and the data priors, allowing for fast inference. However, in cases of acute degradation where information is irreversibly lost, MMSE-based methods tend to produce washed-out reconstructions that lack high-frequency details. Essentially, the MMSE solution can be thought of as the average of all potential solutions, i.e., the conditional mean of the posterior distribution  $\mathbb{E}[\mathbf{x}|\mathbf{y}]$  [18].

Later, the advent of generative models, notably Generative Adversarial Networks (GANs) [19], Variational Autoencoders (VAEs) [20] and diffusion model [21], along with their popular variants [22]–[25], have brought DL-based IR methods to unprecedented heights. Their strength lies in their ability to produce perceptually realistic results from a meaningful latent space. Similarly to Eq. 2, given a pre-trained generative model  $\mathcal{G}(\star)$ , the optimization objective can be formulated as:

$$\arg \min_{\mathbf{w}} \frac{1}{2\sigma^2} \|\mathcal{A}\mathcal{G}(\mathbf{w}) - \mathbf{y}\|_2^2 + \lambda\mathcal{R}(\mathbf{w}) \quad (3)$$

where  $\mathbf{w}$  is the latent variables,  $\mathcal{G}(\mathbf{w})$  is the generated samples conditioned on  $\mathbf{w}$ , and  $\mathcal{R}(\mathbf{w})$  is the data prior that regularizing  $\mathbf{w}$  to its original distribution space.

**Diffusion Models and Their Limitations:** Diffusion models have recently outperformed GANs and emerged as the new

state-of-the-art (SOTA) generative models [28]. To start with, most current studies on diffusion models are primarily focused on three main formulations [29], [30]: denoising diffusion probabilistic models (DDPMs) [21], [31], [32], score-based generative model (SGMs) [24], [33], and stochastic differential equations (SDEs) [25], [34]. Among them, DDPMs and SGMs can be generalized to a scenario with infinite time steps or noise levels and can be described using SDEs. Importantly, all the formulations mentioned above are trained to model the Markov transition from a simple distribution, e.g., gaussian distribution, to a complex data distribution. This process is facilitated by a learned score function [35], [36] that assesses the likelihood of intermediate transition probability distributions, enabling the generation of samples through a series of controlled stochastic processes. Unlike the MMSE-based method, the solutions of diffusion can be considered as sampling from the posterior distribution  $p(\mathbf{x}|\mathbf{y})$ , thus resulting in better perceptual quality. Recognizing the potential, several studies have started to exploit the capability of diffusion models to address different IR tasks [37]–[40] as well as the LACT problem [41], [42]. To do this, most of those methods keep the training of a diffusion model intact and only modify the inference procedure to generate samples that satisfy realism and consistency. In other words, the pre-trained diffusion model will be capable of addressing any linear inverse problem within the same image space.

It is widely recognized that the reverse sampling process of the diffusion models is often time-consuming due to its dependence on an iterative Monte Carlo Markov Chain (MCMC) process, which requires a few thousand steps to converge. A potential solution to accelerate the sampling could involve taking larger steps toward the desired data distribution in each iteration. However, this approach could potentially derail the sampling process from the beginning due to the inaccurate estimation of the score function in areas of low density. Luo et al. [43] proposed a mean-reverting SDEs (MR-SDEs) that initiates the reverse diffusion process from a Gaussian distribution, with the mean set equal to the observed measurement. This method can significantly reduce the number of iterations required for convergence. However, one remaining question is: Are the constraints imposed by LQ measurements strong enough to produce proper reconstruction? The answer is generally negative. Despite our implementation of mean-reverting strategies to narrow down the possible solutions, numerous candidate HQ images could still explain the observed LQ measurements, particularly in cases of severe degradation.

Therefore, an additional consistency constraint will be needed to address the above issues, highlighting another challenge associated with the diffusion model, i.e., the perceptual-distortion tradeoff [44]. Several studies have revealed that while images restored by diffusion models exhibit superior perceptual quality, they may not perform as well on fidelity metrics such as SSIM and PSNR [18], [45], [46]. The Range-Null space decomposition (RNSD) [37], [47] presents a novel solution for balancing realism with consistency: This method leverages the diffusion model to produce realistic content in the null-space and analytically ensures data consistency in the range-space. We believe the

RNSD could be an ideal tool to guide reverse diffusion in the case of MR-SDEs.

**Our Proposed Work:** Inspired by these approaches, in this paper, we propose a novel approach to combine the RNSD and MR-SDE for better LACT reconstruction. given a limited-angle sinogram, we first employ a vanilla method (This can be any end-to-end DNNs optimized through Eq. 2 or analytic CT reconstruction algorithms) to obtain a seed reconstruction, which is then utilized to condition and initialize the mean-reverting reverse diffusion process. Note that in LACT, computing the pseudo-inverse analytically, e.g., via Singular value decomposition (SVD), is impractical due to the ill-posed nature of the problem and the high computational cost. Therefore, to guide the reverse diffusion trajectory toward the optimal point in the distribution space, we approximate the Moore-Penrose pseudo-inverse  $\mathbf{A}^\dagger$  [48] of the Radon transform to extract and refine the null-space content during the reverse diffusion process. Since the actual generated content of RN-SDEs is the Residual/Difference between the HQ and LQ image pairs, we name our proposed method as *Residual Null-Space Diffusion Stochastic Differential Equations* (RN-SDEs). To summarize, our main contributions are as follows:

- We proposed RN-SDEs, a diffusion model that use NafNet [49] as the diffusion backbone, combining *mean-reverting SDEs (MR-SDEs)* [43] and *the range-null space decomposition (RNSD)*, for fast and high-quality LACT reconstruction.
- We utilize the MMSE (Minimum Mean Square Error) solutions,  $\mathbb{E}[\mathbf{x}|\mathbf{y}]$ , specifically the NafNet reconstructions, as the "mean" in MR-SDEs, significantly enhancing the fidelity of the reconstruction.
- We introduce a universal approach for estimating the pseudo-inverse of Radon transform,  $\hat{\mathbf{A}}_\eta^\dagger$ , and improve the way of applying data consistency in [37] to accommodate the estimation errors.
- We demonstrate the effectiveness of RN-SDEs through ChromSTEM and medical CT datasets. Experimental results indicate we can yield superior perceptual quality while preserving data consistency with RN-SDEs. Moreover, as it can be seen in Figure 2, RN-SDEs are fast during inference, significantly outpacing DOLCE [42], the SOTA for the LACT problem, by hundreds of times, while producing a better quality output.

## II. PRELIMINARIES

### A. Diffusion Stochastic Differential Equations (SDEs)

Diffusion SDEs [25] provide a way to formulate both the forward and reverse processes as the solutions of stochastic differential equations. Specifically, the forward process  $\{\mathbf{x}_t\}_{t=0}^T$  involves perturbing clean data samples  $\mathbf{x}_0 \sim p(\mathbf{x}_0)$  to a noisified version  $\mathbf{x}_T \sim p(\mathbf{x}_T)$  governed by the following SDE [25]:

$$d\mathbf{x} = \mathbf{f}(\mathbf{x}, t)dt + g(t)d\mathbf{w} \quad (4)$$

where  $\mathbf{w}$  denotes a standard Wiener process,  $\mathbf{f}(\star)$  is a function of  $\mathbf{x}$  and  $t$  that computes the drift coefficient, and  $g(\star)$  is a

time-dependent function that computes the diffusion coefficient. Normally, the final state  $\mathbf{x}_T$  is expected to follow a Gaussian distribution characterized by a predefined mean and variance. Note that DDPMs [21] and SGMs [24] can be easily generalized into this framework by replacing the drift and diffusion coefficients (see Appx. A).

To reverse the above process and sample data from noise. Anderson [50] shows that a corresponding reverse version exists for any forward SDEs defined in the form of Eq. 4. This reverse SDE runs in the reverse direction but tracks the same marginal distribution  $q(\mathbf{x}_t)$ , which can be written as:

$$d\mathbf{x} = [\mathbf{f}(\mathbf{x}, t) - g(t)^2 \nabla_{\mathbf{x}} \log p(\mathbf{x}_t)] dt + g(t)d\bar{\mathbf{w}} \quad (5)$$

where  $\bar{\mathbf{w}}$  is a reverse-time Wiener process.  $\nabla_{\mathbf{x}} \log p(\mathbf{x}_t)$  is the score function, which indicates the direction that maximizes the likelihood of the distribution. Typically, the score function is estimated by a neural network  $\mathbf{s}_\phi(\mathbf{x}, t)$  and optimized using the following score matching [51]–[53] objectives which can be directly estimated from the training data  $\mathbf{x}_0$ :

$$\mathbb{E}_{t \in \mathcal{U}} \mathbb{E}_{p(\mathbf{x}_t)} [||\nabla_{\mathbf{x}} \log p(\mathbf{x}_t|\mathbf{x}_0) - \tilde{\mathbf{s}}_\phi(\mathbf{x}_t, \mu, t)||], \quad (6)$$

where  $\mathcal{U}$  denotes a uniform distribution over the time interval  $[0, T]$ . Once trained, the learned score function can be plugged into Eq. 5 to simulate the reverse stochastic process from  $\mathbf{x}_T$  back to  $\mathbf{x}_0$ . This simulation is carried out using numerical SDE solvers, such as the Euler-Maruyama, Milstein, and stochastic Runge-Kutta methods.

### B. Range-Null Space Decomposition (RNSD) via $\mathbf{A}^\dagger$

For a linear operator  $\mathbf{A} \in \mathbb{R}^{m \times n}$ , its pseudo-inverse  $\mathbf{A}^\dagger$  satisfies the Moore-Penrose conditions, with  $\mathbf{A}\mathbf{A}^\dagger\mathbf{A} \equiv \mathbf{A}$  being one of the critical properties for our discussion.

- **Range-Space Projection:** The product  $\mathbf{A}^\dagger\mathbf{A}$  acts as a range-space projector, mapping any vector  $\mathbf{x} \in \mathbb{R}^n$  onto the range-space of  $\mathbf{A}$ , ensuring it corresponds to a vector in  $\mathbf{A}$ 's column space.
- **Null-Space Projection:** The matrix  $\mathbf{I} - \mathbf{A}^\dagger\mathbf{A}$  will serve as a null-space projector, mapping any vector  $\mathbf{x}$  onto the corresponding null space of  $\mathbf{A}$ . This guarantees that the projection,  $(\mathbf{I} - \mathbf{A}^\dagger\mathbf{A})\mathbf{x}$ , is orthogonal to the range space, *i.e.*, representing the orthogonal complement of the range space in the full space.
- **IR Perspective:** Given an HQ image  $\mathbf{x}$ , the range-space contains the uncorrupted information that must be preserved during restoration. Conversely, the null-space contents highlight the information orthogonal to  $\mathbf{A}$ 's range-space, affected by the degradation operation  $\mathbf{A}$ . These orthogonal components emerge as potential candidates for correction or refinement during restoration. Noteworthy, by further processing the range/null-space contents with  $\mathbf{A}$ , the processed null-space contents will become 0 (*i.e.*,  $\mathbf{A}\mathbf{A}^\dagger\mathbf{A}\mathbf{x} \equiv 0$ ) while the processed range-space contents will become  $\mathbf{y}$  (*i.e.*,  $\mathbf{A}(\mathbf{I} - \mathbf{A}^\dagger\mathbf{A})\mathbf{x} \equiv \mathbf{y}$ ).

Leveraging these properties, any vector  $\mathbf{x}$  can be represented as a composite of its components within the range-space and



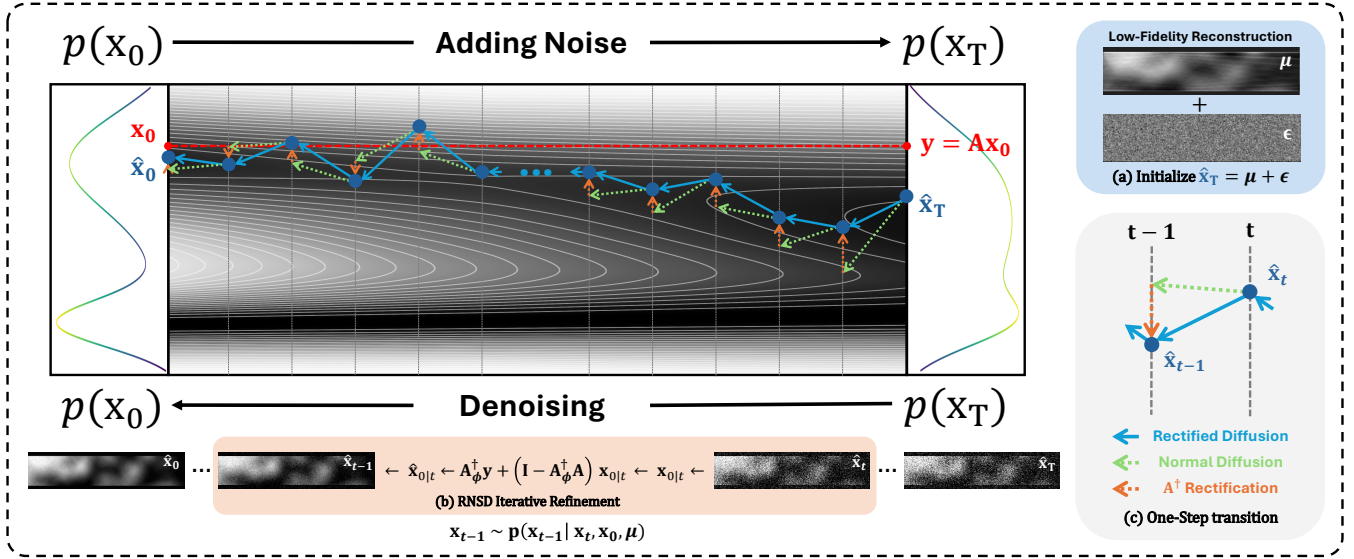


Fig. 3. Visualization of our RN-SDE denoising diffusion process for LACT reconstruction. (a) initialize the terminal state  $\hat{x}_T$  of diffusion as the summation of a low-quality reconstruction  $\mu$  and a Gaussian noise  $\epsilon$ , This step strategically positions the starting point of the reverse diffusion closer to  $\mathbf{x}_0$  within the distribution space, facilitating a more effective and accurate convergence towards the ground truth image during the denoising stage; (b) illustrates the rectification mechanism involved in the reverse diffusion process, where we applied range-null space decomposition (RNSD) to the intermediate clean prediction  $\mathbf{x}_{0|t}$  to enforce data consistency; (c) shows the dynamics of a single transition step in the denoising process. Providing a visual example of how the RNSD-based rectification effectively reduces stochasticity during the reverse diffusion process.

null-space. This leads to the formulation of the following equation:

$$\mathbf{x} \equiv \mathbf{A}^\dagger \mathbf{A} \mathbf{x} + (\mathbf{I} - \mathbf{A}^\dagger \mathbf{A}) \mathbf{x} \quad (7)$$

which reveals the inherent partition of the vector space induced by  $\mathbf{A}$ . This simple decomposition is significant in analyzing linear inverse problems (IR) and will be further explored in subsequent sections.

### III. METHOD

#### A. LACT Range-Null Space Decomposition

In this paper, we will consider a simpler, noise-free scenario of LACT Reconstruction:

$$\mathbf{y} = \mathbf{A} \mathbf{x} \quad (8)$$

where  $\mathbf{x} \sim p(\mathbf{x})$  is an image sampled from the ground-truth (GT) data distribution,  $\mathbf{A}$  denotes the Radon transform, and  $\mathbf{y}$  is the limited-angle sinogram, where the angle  $\theta$  is limited such that  $0 \leq \theta \leq \theta_{\max}$  with  $\theta_{\max} < \pi$ . Referring to Eq. 3, our objective is to yield an estimation,  $\hat{\mathbf{x}}$ , that satisfy both the consistency constraint,  $\mathbf{A} \hat{\mathbf{x}} = \mathbf{y}$ , and the realness constraints,  $\hat{\mathbf{x}} \sim p(\mathbf{x})$ . Among them, the consistency constraint can be analytically guaranteed within the range-space of  $\mathbf{A}$  by solving:

$$\mathbf{A}^\dagger \mathbf{y} = \mathbf{A}^\dagger \mathbf{A} \bar{\mathbf{x}}, \quad (9)$$

where  $\mathbf{A}^\dagger$  is the Moore-Penrose pseudo-inverse of the Radon transform. The solution  $\bar{\mathbf{x}}$  is not unique; it only ensures that the sinogram of the reconstructed image matches the GT image for the available angles,  $\theta \in [0, \theta_{\max}]$ . More importantly, since the consistency constraint is only related to the range-space – which is completely independent of the

null-space. We can utilize the diffusion models to generate suitable null-space content,  $(\mathbf{I} - \mathbf{A}^\dagger \mathbf{A}) \hat{\mathbf{x}}$ , that allows the final solutions,  $\hat{\mathbf{x}} = \mathbf{A}^\dagger \mathbf{y} + (\mathbf{I} - \mathbf{A}^\dagger \mathbf{A}) \hat{\mathbf{x}}$ , to fulfill the realness constraint. Notably, the solution  $\hat{\mathbf{x}}$  is a subset of  $\bar{\mathbf{x}}$ , i.e.,  $\hat{\mathbf{x}} \subset \{\mathbf{x} \in \bar{\mathbf{x}} | \mathbf{x} \sim p(\mathbf{x})\}$ , where  $\bar{\mathbf{x}}$  is the set of solutions that meet the consistency constraints.

#### B. Residual Null-Space Stochastic Differential Equation (RN-SDE)

**Forward MR-SDE:** Luo et al. [43], construct the MR-SDEs as a special case of the SDEs discussed in Sec. II-A. To make the mean *reversible*, they formulate the forward SDE [43] as:

$$d\mathbf{x} = \theta_t (\mu - \mathbf{x}) dt + \sigma_t d\mathbf{w} \quad (10)$$

where  $\theta_t, \sigma_t$  time-dependent parameters that respectively regulate the pace of mean-reversion and the noise perturbation and  $\mu$  is the mean of the terminal state, which, in the context of IR, usually indicate the LQ images. In the LACT problem, directly setting the sinogram as  $\mu$  is infeasible due to the dimensional discrepancy between sinograms and images. A typical workaround [15], [42] is to replace the sinogram with a low-fidelity reconstruction, derived from standard inversion methods, such as FBP. Specifically, we incorporate an additional NafNet [49] block for post-processing. This model is optimized with the MMSE objective and the outcomes will be used as  $\mu$  to condition the reverse diffusion process. We demonstrate in Sec. IV that this novel post-processing step can effectively harness the precise low-frequency information from MMSE solutions to improve the reconstruction fidelity.

Following the setting in [43], we define  $\theta_t := \int_0^t \theta_z dz$  and set  $\sigma_t^2 / \theta_t = 2\lambda^2$  for all times  $t$ , where  $\lambda^2$  is the fixed variance.

Given the starting state  $\mathbf{x}_0$ , we can sample  $\mathbf{x}_t$  at any arbitrary time  $t$  from the following Gaussian distribution:

$$p(\mathbf{x}_t|\mathbf{x}_0) = \mathcal{N}(\mathbf{x}_t|m_t(\mathbf{x}_0), v_t) \quad (11)$$

where the mean  $m_t(\mathbf{x}_0)$  and variance  $v_t$  are respectively:

$$m_t(\mathbf{x}_0) := \mu + (\mathbf{x}_0 - \mu)e^{-\bar{\theta}_t} \quad (12)$$

$$v_t := \lambda^2(1 - e^{-2\bar{\theta}_t}). \quad (13)$$

As noted in [43], Equation 11 is described as *mean-reverting* because, as  $t \rightarrow \infty$ , we will have:  $\lim_{t \rightarrow \infty} m_t = \mu$ , and  $\lim_{t \rightarrow \infty} v_t = \lambda^2$ . Consequently, the terminal distribution  $p(\mathbf{x}_T)$  can be approximated by summing up the LQ images  $\mu$  and a Gaussian noise  $\mathcal{N}(0, \lambda^2)$ .

**Reverse the MR-SDE:** To recover the target HQ image from  $\mathbf{x}_T$ , Luo et al. [43] defines the reverse MR-SDE as:

$$d\mathbf{x} = [\theta_t(\mu - \mathbf{x}) - \sigma_t^2 \nabla_{\mathbf{x}} \log p(\mathbf{x}_t)] dt + \sigma_t d\hat{\mathbf{w}}. \quad (14)$$

where the  $\nabla_{\mathbf{x}} \log p(\mathbf{x}_t)$  is the score of the marginal distribution  $p(\mathbf{x}_t)$ . Typically, this score function can be estimated using the score-matching objective mentioned in Sec. II-A. However, the author [43] discovered that this simple objective might lead to an unstable training process. Therefore, they propose an alternative approach to derive an optimum reverse state  $\mathbf{x}_{t-1}$  that maximizes the likelihood of  $p(\mathbf{x}_{t-1}|\mathbf{x}_t, \mathbf{x}_0)$ . Significantly, we found that the modified objective is equivalent to estimating the following score:

$$\nabla_{\mathbf{x}} \log p(\mathbf{x}_t|\mathbf{x}_0)^* = \frac{\mathbf{G}_t \mathbf{x}_t + \mathbf{H}_t \mathbf{x}_0 - (\mathbf{H}_t + \mathbf{G}_t)\mu}{\sigma_t^2 dt} \quad (15)$$

Here, let  $\theta'_t := \int_{t-1}^t \theta_z dz$ , the terms  $\mathbf{G}_t, \mathbf{H}_t$  are respectively:

$$\begin{aligned} \mathbf{G}_t &= \frac{1 - e^{-2\bar{\theta}_{t-1}}}{1 - e^{-2\bar{\theta}_t}} e^{-\theta'_t} - \theta'_t - 1 \\ \mathbf{H}_t &= \frac{1 - e^{-2\theta'_t}}{1 - e^{-2\bar{\theta}_t}} e^{-\bar{\theta}_{t-1}} \end{aligned} \quad (16)$$

The derivation is detailed in Appx. B. To approximate this score, we propose to use Conditional NafNet (Cond-NafNet) [54],  $\mathbf{s}_\phi(\mathbf{x}_t, \mu, t)$ , as the reverse diffusion backbone. This network takes the state  $\mathbf{x}_t$ , the low-fidelity reconstruction  $\mu$ , and time  $t$  as input, and is trained with the commonly-used objective described in Eq. 6.

**RNSD-Based Iterative Refinement:** During inference, we iteratively simulate the reverse stochastic process from  $\mathbf{x}_T$  back to  $\mathbf{x}_0$ . In the distribution space, the mean-reverting strategy allows us to initialize  $\hat{\mathbf{x}}_T$  from a position closer to the ground truth (GT) solution. This leads to a situation where reverse diffusion is more likely to converge to the GT solution despite the randomness of the inference process. Nevertheless, when the distribution  $p(\mu)$ , differs significantly from  $p(\mathbf{x}_0)$ , i.e., in certain LACT tasks where a large number of angles are missing, the stochasticity of the reverse diffusion process can also possibly harm the consistency of the data. To address this issue, similar to [37], we propose to enforce data consistency directly through the RNSD. This is achieved by incorporating

an additional rectification into the estimated score at each time step. To be more precise, we first utilize the estimated score, denoted by  $\mathbf{s}_\phi(\mathbf{x}_t, \mu, t)$ , to generate a clean intermediate state  $\mathbf{x}_{0|t}$ , which is given by:

$$\mathbf{x}_{0|t} = -\frac{\mathbf{G}_t}{\mathbf{H}_t} \mathbf{x}_t + \frac{\sigma_t^2}{\mathbf{H}_t} \mathbf{s}_\phi(\mathbf{x}_t, \mu, t) dt + (1 + \frac{\mathbf{G}_t}{\mathbf{H}_t})\mu. \quad (17)$$

This intermediate state can be interpreted as a rough estimation of  $\mathbf{x}_0$  at time  $t$ . Later, we decompose  $\mathbf{x}_{0|t}$  into  $\mathbf{A}$ 's range and null space. To promote the data consistency, we replace the range-space contents with  $\mathbf{A}^\dagger \mathbf{y}$ , while preserving the null-space contents,  $(\mathbf{I} - \mathbf{A}^\dagger \mathbf{A})\mathbf{x}_{0|t}$ , unchanged. In such a way, the data consistency can be strictly ensured by the combined solution  $\hat{\mathbf{x}}_{0|t}$ , which is given by:

$$\hat{\mathbf{x}}_{0|t} = \mathbf{A}^\dagger \mathbf{y} + (\mathbf{I} - \mathbf{A}^\dagger \mathbf{A})\mathbf{x}_{0|t}. \quad (18)$$

Finally, the rectified clean estimation  $\hat{\mathbf{x}}_{0|t}$  will be inserted into the reverse MR-SDE to sample the next state  $\mathbf{x}_{t-1}$  from the modified conditional distribution  $p(\mathbf{x}_{t-1}|\mathbf{x}_t, \hat{\mathbf{x}}_{0|t})$ . This process can be described using the reverse RN-SDE, which we defined as:

$$d\mathbf{x} = (\mathbf{G}_t + \theta_t dt)(\mu - \mathbf{x}_t) + \mathbf{H}_t(\mu - \hat{\mathbf{x}}_{0|t}) + \sigma_t d\hat{\mathbf{w}}, \quad (19)$$

Importantly, since the realness is already guaranteed by the maximum-a-posteriori objective during training, by iterating through Eq. 17, Eq. 18, and Eq. 19 from  $T$  to 1, we can obtain a clean reconstruction  $\hat{\mathbf{x}}_0$  that satisfies both consistency and realness constraints.

**Time-Travel Trick:** Except for the above iterative refinement pipeline, [37] propose a time-travel trick to address the *inferior Realness* caused when the range-space contents are too local or uneven. As the name suggests, during sampling ( $\mathbf{T} \rightarrow 0$ ), we travel backward from a chosen time-step,  $t$ , to the past,  $t+l$ . Due to the iterative refinement process, the **past** state  $\mathbf{x}_{t+l}$ , which we sampled from  $q(\mathbf{x}_{t+l}|\mathbf{x}_t)$ , will be more accurate than the real past state. Therefore, as we return to the current time-step  $t$  again through the RN-SDE sampling iteration (Eq. 17, Eq. 18, and Eq. 19), we obtain a better  $\mathbf{x}_t$ .

This process is controlled by three hyperparameters: The length of time we travel back each time,  $l$ , the number of times we repeat the same time interval,  $r$ , and the total number of diffusion steps,  $\mathbf{T}$ . Typically, the actual number of time-steps  $\mathbf{T}_{tt}$  that the sampling with time traveling goes through can be measured by the equation below:

$$\mathbf{T}_{tt} = \mathbf{T} + 2l(r-1) \left\lfloor \frac{\mathbf{T}-1}{l} \right\rfloor + 1 \quad (20)$$

When  $r = 1$  and  $l = 1$ , the sampling process with time traveling will be equivalent to the normal sampling process. However, a major drawback of this trick is that even when we set the minimum repetition time, i.e.,  $r = 2$ , the actual sampling step number  $\mathbf{T}_{tt}$  will still be almost three times the original  $\mathbf{T}$ . Fortunately, using MR-SDE, we can keep  $\mathbf{T}_{tt}$  within a reasonable range.

**Error Compensation Through Range-Space Scaling:** During the experiment, we notice that the above iterative refinement sometimes tends to over-denoise the images, resulting in inferior reconstructions. We hypothesize the core issue may stem from the inaccurate estimation of  $\hat{\mathbf{A}}_\eta^\dagger$ , which introduces an additional error  $\mathbf{n}$  to the rectified clean image,  $\hat{\mathbf{x}}_{0|t} = \mathbf{x}_{0|t} - \hat{\mathbf{A}}_\eta^\dagger(\mathbf{A}\mathbf{x}_{0|t} - \mathbf{y}) + \mathbf{n}$ . This typically accompanies two problems: 1) The error  $\mathbf{n}$  may not follow a Gaussian distribution, and the scale of the noise is not measurable; 2) When additional error  $\mathbf{n}$ , other than the anticipated noise  $\sigma_t d\hat{\mathbf{w}}$ , is introduced, the pretrained model will become unable to predict the intermediate clean images  $\mathbf{x}_{0|t-1}$  accurately. Furthermore, errors in  $\mathbf{x}_{0|t-1}$  will continuously accumulate, undermining the subsequent reverse diffusion process. To mitigate the impact of the error, we rescale the range-space correction  $\hat{\mathbf{A}}_\eta^\dagger(\mathbf{A}\mathbf{x}_{0|t} - \mathbf{y})$  by a rescaling factor  $\Gamma_t$ , which is given by:

$$\hat{\mathbf{x}}_{0|t} = \mathbf{x}_{0|t} - \Gamma_t \hat{\mathbf{A}}_\eta^\dagger(\mathbf{A}\mathbf{x}_{0|t} - \mathbf{y}). \quad (21)$$

Here, we assign a hyperparameter  $\alpha$  to control the rescaling operation and formulate  $\Gamma_t$  to be  $\frac{\alpha\sigma_t\sqrt{dt}}{\mathbf{H}_t}\mathbf{I}$ . This minor adjustment allows us to modify Eq. 19 into:

$$\mathbf{x}_{t-1} = \mathbf{H}_t \hat{\mathbf{x}}_{0|t} + \mathbf{C} + \sigma_t \sqrt{dt}(\alpha \mathbf{n} + \epsilon_t), \quad \epsilon_t \sim \mathcal{N}(0, \mathbf{I}) \quad (22)$$

where  $\sqrt{dt}\epsilon_t = d\hat{\mathbf{w}}$  and  $\mathbf{C}$  represents the remaining terms that do not involve  $\mathbf{x}_0$  and the noise. During sampling, this factor is crucial for stabilizing the reverse process. Choosing a smaller  $\alpha$  can minimize the impact of  $\mathbf{n}$ , but this at the same time also weakens the range-space correction, resulting in worse data consistency.

Apart from the rescaling, we empirically found that inserting unguided iterations, i.e., those without data consistency term, between guided iterations can effectively prevent the accumulation of errors. In practice, we skip the consistency term at specific iterations, with the frequency of skipping regulated by an extra hyperparameter  $\beta$ . In this paper, we focus on the LACT problem, where  $\mathbf{A}^\dagger$  needs to be estimated with a neural network. The skipping trick mentioned above is not required for other simpler IR tasks, where the pseudo-inverse can be numerically calculated, such as image inpainting and colorization. The algorithm details are shown in Algo. III-B.

**Estimate the Pseudo-Inverse of Radon:** One remaining issue is estimating the Radon’s Moore-Penrose pseudo-inverse  $\mathbf{A}^\dagger$ . Conventional numerical approaches for computing this inverse are typically infeasible, primarily due to the computation complexity caused by large-scale matrix operations and the ill-posed nature of the LACT problem. Here, we present a trainable method to estimate the pseudo-inverse of Radon using a simple objective.

In our study, we implement the Radon pseudo-inverse  $\mathbf{A}^\dagger$  using a **Learnable Back-Projection**<sup>2</sup> block combined with a **Non-bias NafNet** [49] for post-processing (Fig. 4). The learnable back-projection block applies a learned Ramp filter  $\omega_\eta$  to filter the input sinograms and subsequently back-projects them to the image domain, allowing us to resolve

<sup>2</sup>Refer to Appx C for more details.

---

#### Algorithm 1 Sampling Process of RN-SDE

---

**Require:** The low-fidelity reconstruction  $\mu$ , the degradation operator  $\mathbf{A}$ , the learned pseudo-inverse  $\hat{\mathbf{A}}_\eta^\dagger$ , the rescaling factor  $\alpha$ , and the skipping factor  $\beta$

```

1:  $\mathbf{x}_T \sim \mathcal{N}(\mu, \lambda^2)$ 
2: for  $t = T, \dots, 1$  do
3:    $\mathbf{x}_{0|t} = -\frac{\mathbf{G}_t}{\mathbf{H}_t} \mathbf{x}_t + \frac{\sigma_t^2}{\mathbf{H}_t} \mathbf{s}_\phi(\mathbf{x}_t, \mu, t) dt + (1 + \frac{\mathbf{G}_t}{\mathbf{H}_t}) \mu$ ,
4:   if  $t \bmod \beta \neq 0$  then
5:      $\hat{\mathbf{x}}_{0|t} = \mathbf{x}_{0|t} - \Gamma_t \hat{\mathbf{A}}_\eta^\dagger(\mathbf{y}_{0|t} - \mathbf{y})$ ,    $\Gamma_t = \frac{\alpha\sigma_t\sqrt{dt}}{\mathbf{H}_t} \mathbf{I}$ 
6:   else
7:      $\hat{\mathbf{x}}_{0|t} = \mathbf{x}_{0|t}$ ,
8:   end if
9:    $\mathbf{x}_{t-1} \sim p(\mathbf{x}_{t-1} | \mathbf{x}_t, \hat{\mathbf{x}}_{0|t})$ ,            $\Rightarrow$  Equation 22
10: end for
11: return  $\mathbf{x}_0$ 

```

---

the dimensional discrepancy between sinograms and images. The post-processing with NafNet refines the back-projection results, yielding more accurate estimations. To train such a model, we set the training objective to minimize the square error between  $\mathbf{A}$  and  $\mathbf{A}\hat{\mathbf{A}}_\eta^\dagger\mathbf{A}$ . Interestingly, the data consistency term, Eq. 18, monotonically relies on the property:  $\mathbf{A}\mathbf{A}^\dagger\mathbf{A} \equiv \mathbf{A}$ , which is enforced by  $\ell_1(\hat{\mathbf{A}}_\eta^\dagger)$ , we found out that the property  $\mathbf{A}^\dagger\mathbf{A}\mathbf{A}^\dagger \equiv \mathbf{A}^\dagger$  is also crucial for maintaining data fidelity during the diffusion sampling. Therefore, we incorporate  $\ell_2(\hat{\mathbf{A}}_\eta^\dagger)$  into the final objective function  $\ell_{\text{pseudo}}$ , yielding:

$$\begin{aligned} \ell_1(\hat{\mathbf{A}}_\eta^\dagger) &= \mathbb{E}_{\mathbf{x} \sim p(\mathbf{x}_0)} [\|\mathbf{A}\mathbf{x} - \mathbf{A}\hat{\mathbf{A}}_\eta^\dagger\mathbf{A}\mathbf{x}\|] \\ \ell_2(\hat{\mathbf{A}}_\eta^\dagger) &= \mathbb{E}_{\mathbf{y} \sim p(\mathbf{y})} [\|\hat{\mathbf{A}}_\eta^\dagger\mathbf{y} - \hat{\mathbf{A}}_\eta^\dagger\mathbf{A}\hat{\mathbf{A}}_\eta^\dagger\mathbf{y}\|] \\ \ell_{\text{pseudo}} &= (1 - \alpha)\ell_1(\hat{\mathbf{A}}_\eta^\dagger) + \alpha\ell_2(\hat{\mathbf{A}}_\eta^\dagger) \end{aligned} \quad (23)$$

Here,  $\hat{\mathbf{A}}_\eta$  denotes the simulated Radon pseudo-inverse with learnable parameters  $\eta$  and  $\alpha \in [0, 1]$  is simply a weighting factor controls the trade-off between those two terms. This model can be optimized via stochastic gradient descent. In practice, we recommend setting  $\alpha$  to 0.2 to allocate more importance to  $\ell_1$ , or initially using only  $\ell_1$  during the early stages of training, and fine-tuning the model with a balanced loss for best training efficiency.

## IV. EXPERIMENTS

In this section, we present our experimental setup and results, comprehensively evaluating our proposed method against several SOTA methods. In quantitatively comparing different methods, we consider several widely used metrics, including the standard distortion metrics peak signal noise ratio (PSNR) and structural similarity index measure (SSIM), as well as the popular perceptual metric, Learned Perceptual Image Patch Similarity (LPIPS) [27]. Considering the computational and time costs, we will primarily conduct subsequent experiments using the ChromSTEM dataset, while the public C4KC-KiTS [26] dataset will be introduced as a complement in Sec IV-D to further show the effectiveness and generalizability of our method.

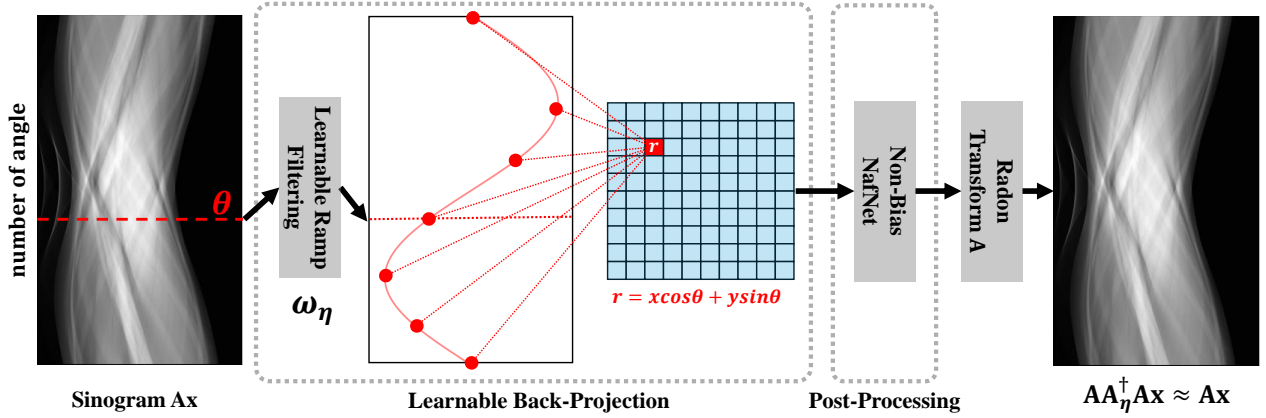


Fig. 4. Implementation of Radon Moore-Penrose pseudo-inverse  $A_\eta^\dagger$ . It mainly consists of two blocks: The first is the learnable back-projection block, where we apply a learnable transformation to the Ramp filter and filter the input sinogram  $Ax$ . Then, we back-project the image from the sinogram domain to the image domain. The second block uses a non-bias NafNet to perform post-processing on the back-projection results and outputs  $A^\dagger Ax$ .

### A. Dataset And Preprocessing Procedures

**ChromSTEM Dataset:** The *Chromatin electron scanning transmission electron microscopy (ChromSTEM)* dataset is synthesized using the SR-EV [55] model, designed by the Northwestern University Center for Chromatin NanoImaging in Cancer. Based on current knowledge of chromatin’s structural and statistical characteristics, SR-EV effectively simulates the three-dimensional structure of chromatin, demonstrating a high degree of visual similarity to real data samples. The dataset comprises 1196 synthesized 3D chromatin structures of stem cells. Each chromatin structure consists of 256 slices that are  $50 \times 256$  pixels in size, with 2 nm spatial resolution. To facilitate network training, a random sample of approximately 17,200 sub-volumes with 16 channels from these 3D structures are selected and zero-padded to  $64 \times 256$ . Their corresponding sinograms are limited to the size of  $91 \times 256$  to fully simulate the real ChromSTEM imaging scenario, where a projection is obtained every  $2^\circ$  across the  $[0^\circ, 180^\circ]$  interval. Finally, a random selection of 24 sub-volumes from distinct chromatin structures is chosen as the testing set, while the remaining sub-volumes are utilized for training. Access to the ChromSTEM dataset is available in our project repository.

**C4KC-KiTS Dataset:** To better compare our method with other SOTA methods, such as DOLCE [42], we utilized the *Kidney CT scans from the publicly available 2019 Kidney and Kidney Tumor Segmentation Challenge (C4KC-KiTS)* [26] dataset. The C4KC-KiTS dataset contains approximately 70,000 2D body scans of size  $512 \times 512$ , covering a range of anatomical regions from the chest to the pelvis. Unfortunately, since DOLCE does not publish the complete partitioning of the training and test sets, we can not compare their results directly. To make a fair comparison, we adhered to the DOLCE projection setup, resulting in sinograms of size  $720 \times 512$ , i.e., a uniform scanning of every  $0.25^\circ$ . Besides, in this paper, the CT intensity is clipped to the range of  $[-250, 500]$  HU following [56], and then normalized to  $[0, 1]$ . We randomly selected 24 body scans from different patients for testing and used the remaining images for training.

### B. Implementation Details

The model backbone utilized in RN-SDE is the Cond-NafNet [54], which we provide details in Appx. D. For the two datasets mentioned above, we evaluate our proposed RN-SDE based on three missing angles, i.e.,  $\theta_{miss} \in \{60^\circ, 90^\circ, 120^\circ\}$ , training individual models for each LACT scenario.

For the noise schedules of diffusion, we follow the default setting of [43], fixing  $\lambda$  while varying  $\theta$  according to the cosine schedule. Specifically, for the ChromSTEM dataset, to validate the impact of using different  $\mu$  on the final reconstruction results, we experimented with different time steps  $\mathbf{T}$  (Shown in Table. I) and selected the one that performed best on the LPIPS metric for subsequent experiments. For the C4KC-KiTS dataset, we used the same  $\mathbf{T}$  to demonstrate that the choice of  $\mathbf{T}$  will not significantly impact the final reconstruction. For the inference process, given the advantages of RN-SDE, we need far fewer time steps to achieve competitive results than the normal DDPM diffusion. Therefore, we adopted the most widely used DDPM [21] sampling method, i.e., using the same number of diffusion steps  $\mathbf{T}$  as in training, to obtain the best reconstruction results.

For training, all models are implemented based on PyTorch and trained on a single Nvidia Quadro RTX 8000 GPU with single precision (float 32). We use the AdamW optimizer while the learning rate is initialized to be  $5 \times 10^{-4}$  and controlled by the Cosine Annealing scheduler. The batch size is set to 8 for all experiments.

### C. Ablation Study

**Ablation Study on Time Steps with Mean-Reverting.** We highlighted that the mean-reverting diffusion strategy effectively reduces the number of steps required during the actual reverse diffusion process. To validate the effectiveness of this strategy, we retrained the network using different values of  $\mathbf{T}$  across three distinct LACT scenarios on the ChromSTEM dataset, conducting sampling without applying the RNSD-based rectification. We report the average result of the 10 sampling runs in Table I. As anticipated, we observe a significant improvement in distortion-based metrics as  $\mathbf{T}$  increases. However, this improvement noticeably slows once



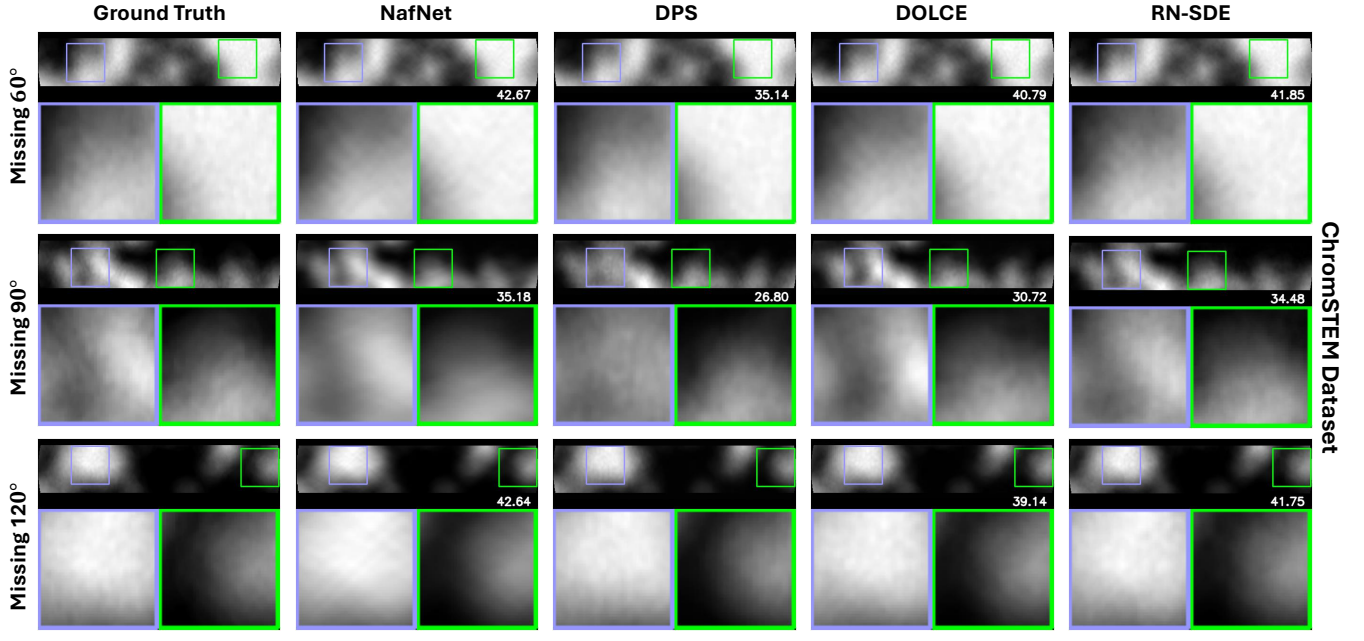


Fig. 5. Visual evaluation of limited angle tomographic reconstruction on the ChromSTEM test set using FBP, NafNet, DPS, DOLCE, and our RN-SDEs. From top to bottom, we present the visualization of a typical reconstruction result for  $\theta_{miss} \in \{60^\circ, 90^\circ, 120^\circ\}$ . The bottom right corner of each example shows the corresponding PSNR metric compared to the Ground Truth (first column).

$\mathbf{T}$  approaches 200. From a perceptual perspective, the best performance typically occurs at  $\mathbf{T} = 100$ , indicating that this value is sufficient to ensure the convergence of the diffusion process. Considering these factors, we set  $\mathbf{T}$  to 200 by default in all subsequent experiments unless otherwise specified.

TABLE I  
AVERAGE PSNR/SSIM/LPIPS RESULTS OF RN-SDE (W/O RNSD RECTIFICATION) TRAINED WITH DIFFERENT TIME STEPS ON CHROMSTEM TEST IMAGES

$\mathbf{T}$	$60^\circ$			$90^\circ$			$120^\circ$		
	PSNR $\uparrow$	SSIM $\uparrow$	LPIPS $\downarrow$	PSNR $\uparrow$	SSIM $\uparrow$	LPIPS $\downarrow$	PSNR $\uparrow$	SSIM $\uparrow$	LPIPS $\downarrow$
50	36.50	0.905	0.0932	36.01	0.889	0.1045	33.27	0.860	0.1138
100	41.77	0.972	0.0097	38.96	0.955	0.0072	35.07	0.931	0.0112
200	42.08	0.975	0.0062	39.12	0.958	0.0080	35.17	0.933	0.0125
500	42.24	0.976	0.0110	39.20	0.959	0.0109	35.19	0.935	0.0130
1000	42.45	0.976	0.0162	39.16	0.957	0.0229	35.20	0.935	0.0163

**Ablation Study with different  $\mu$  and Incorporating RNSD Data-Consistency.** As previously mentioned, in RN-SDE, we utilize the accurate low-frequency information provided by  $\mathbb{E}[\mathbf{x}|\mathbf{y}]$  to control and guide the mean-reverting diffusion process, which undoubtedly improves the quality of image restoration. However, this requires additional training of a NafNet, which incurs extra time costs. We question whether a more accessible modality could be used as  $\mu$  while entrusting the data consistency to RNSD rectification. For this purpose, we further evaluate our method by adopting FBP reconstruction as  $\mu$  for mean-reverting. For different  $\mu$ , we experimented with two situations: with (w/) and without (w/o) the RNSD-based data-consistency measurement ( $\mathbf{A}^\dagger$ ) provided in Eq. 18. For simplicity, we refer to the group of experiments using FBP reconstruction as  $\mu$  to be **FBP-MR**, and those using NafNet

reconstruction as **NAF-MR**.

TABLE II  
ABLATION STUDY ON MEAN-REVERTING STRATEGIES AND RNSD-BASED RECTIFICATION

Angle	$60^\circ$			$90^\circ$			$120^\circ$		
	PSNR $\uparrow$	SSIM $\uparrow$	LPIPS $\downarrow$	PSNR $\uparrow$	SSIM $\uparrow$	LPIPS $\downarrow$	PSNR $\uparrow$	SSIM $\uparrow$	LPIPS $\downarrow$
<i>NAF-MR: NafNet Reconstruction As <math>\mu</math></i>									
w/o $\mathbf{A}^\dagger$	42.51	0.977	0.0078	39.52	0.961	0.0097	35.46	0.939	0.0144
w/ $\mathbf{A}^\dagger$	43.93	0.982	0.0069	40.43	0.965	0.0086	35.62	0.939	0.0143
<i>FBP-MR: FBP Reconstruction As <math>\mu</math></i>									
w/o $\mathbf{A}^\dagger$	35.13	0.936	0.0111	28.46	0.880	0.0269	21.73	0.756	0.0726
w/ $\mathbf{A}^\dagger$	42.73	0.975	0.0053	38.73	0.955	0.0033	29.44	0.872	0.0328

As shown in Table II, without  $\mathbf{A}^\dagger$ , we observed a remarkable decline in reconstruction quality for FBP-MR compared to the NAF-MR. This trend is evident across all metrics and is particularly pronounced in severe LACT scenarios. We attributed this to the sensitivity of MR-SDE to the choice of  $\mu$ . After applying  $\mathbf{A}^\dagger$ , although the results for PSNR and SSIM in the FBP-MR group remain inferior to those of the NAF-MR group, the perceptual quality, as measured by LPIPS, has surprisingly surpassed that of the NAF-MR group. Meanwhile, it is worth mentioning that, **FBP-MR outperforms the current SOTA method, DOLCE**, (Table III) on the  $60^\circ$  and  $90^\circ$  LACT scenarios. Another noticeable change comes from the data consistency term,  $\|\mathbf{A}\hat{\mathbf{x}} - \mathbf{y}\|_2$ , for which we plot its mean and standard deviation in Figure 7. After applying RNSD rectification, the mean and variance notably decrease, indicating the possible solution  $\hat{\mathbf{x}}$  has been constrained to a smaller range, resulting in more stable and accurate reconstructions.

Those observations highlight that the mean-reverting strat-



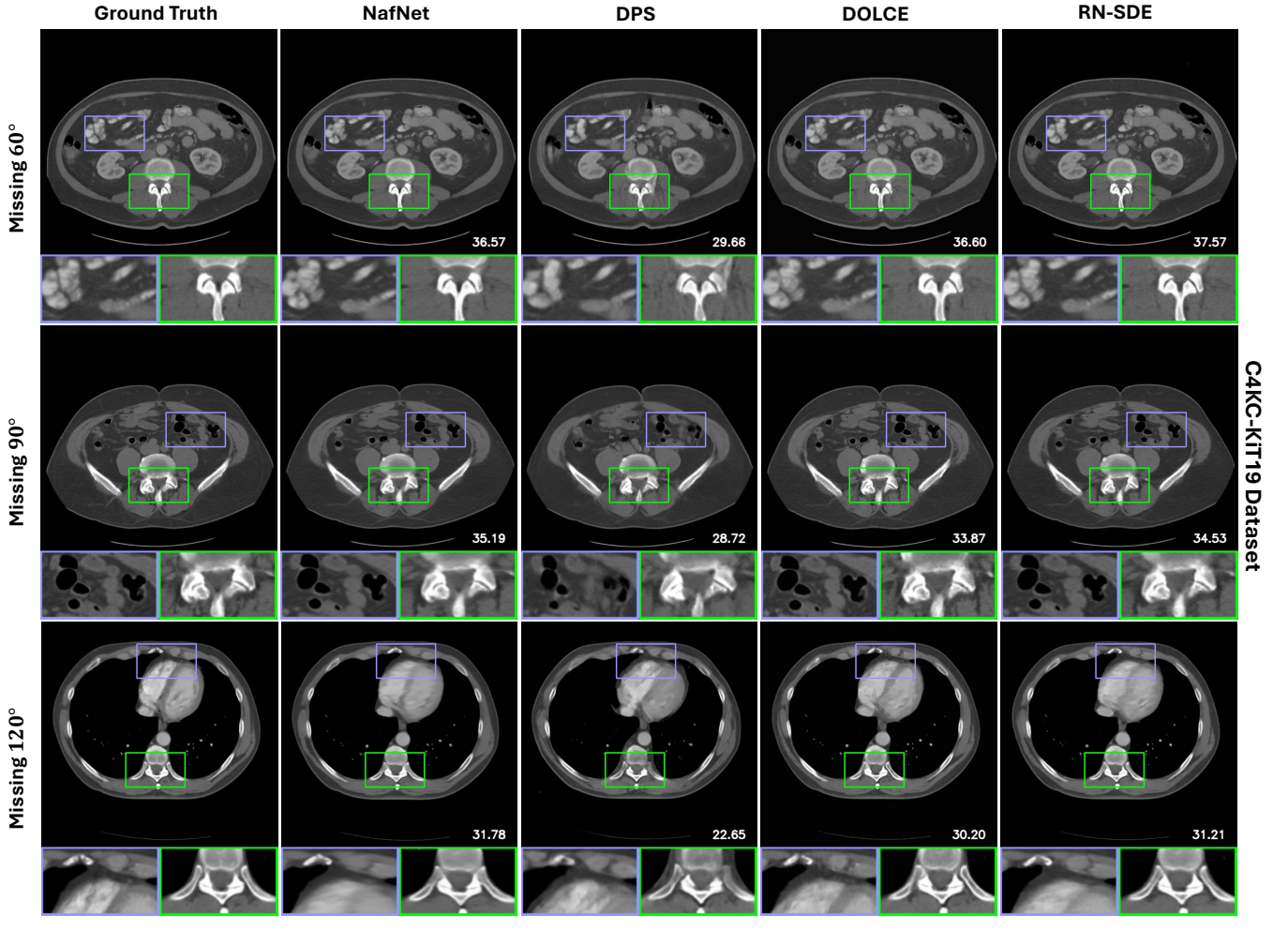


Fig. 6. Visual evaluation of limited angle tomographic reconstruction on the C4KC-KiTS dataset using FBP, NafNet, DPS, DOLCE, and our RN-SDE. From top to bottom, we present the visualization of a typical reconstruction for  $\theta_{miss} \in \{60^\circ, 90^\circ, 120^\circ\}$  respectively. The bottom right corner of each example shows the corresponding PSNR metric compared to the Ground Truth (first column).

egy is highly sensitive to the choice of  $\mu$  and underscore the effectiveness and necessity of incorporating  $\mathbf{A}^\dagger$  for addressing various LACT scenarios. For the subsequent experiments, given the final application scenario of this study, we will still use NAF-MR as the default scheme.

#### D. Evaluation and Comparison on Two Datasets

In this section, we compare RN-SDE with six selected LACT reconstruction methods. Table III presents the ten-run average PSNR, SSIM, and LPIPS results for the selected methods, using test images from both the ChromSTEM and C4KC-KiTS datasets. The chosen methods are categorized into three major groups: classical methods (e.g., FBP, TV [57]), MMSE-based IR methods (e.g., NafNet [49]), and diffusion-based IR methods (DPS [39], DDNM+ [37], and DOLCE [42]).

The TV reconstructions were implemented using TomoPy [58], a publicly available CT reconstruction toolkit. NafNet refers to the original framework without embedding input, and its input is also the FBP reconstruction. As NafNet has been shown to outperform the standard UNet in various image restoration tasks, we have opted not to include

UNet in our comparisons. DDNM+ and DPS are two image restoration algorithms based on unconditioned diffusion. They were originally proposed to address general inverse problems, but not specifically designed for the LACT problem. Notably, DDNM+ also utilizes the RNSD approach to guide the reverse diffusion, hence we used the same pre-trained  $\hat{\mathbf{A}}_\eta^\dagger$  as for our RN-SDE. DOLCE is claimed to be the current SOTA method for the LACT problem. Unlike the previous two methods, DOLCE leverages low-quality reconstruction as the condition during training to endorse better reconstruction quality. It is worth noting that all three diffusion-based methods use DDPM [21] as the foundational diffusion framework, while our RN-SDE is essentially based on stochastic differential equations. Furthermore, for our RN-SDE model, we followed the sampling average (SA) outlined in [59], averaging multiple samples from RN-SDE to approximate  $\mathbb{E}[\mathbf{x}|y]$ . This enhances our reconstruction in terms of the distortion metrics, with the tradeoff of perceptual quality. We denote this as **RN-SDE SA** in the table. The main purpose is to ensure a fair comparison between diffusion-based methods and MMSE-based methods like NafNet. For the ChromSTEM dataset, we conduct a grid

TABLE III  
AVERAGE PSNR/SSIM/LPIPS RESULTS FOR SEVERAL METHODS ON CHROMSTEM AND C4KC-KiTS TEST IMAGES

Dataset	ChromSTEM									C4KC-KiTS								
	60°			90°			120°			60°			90°			120°		
	PSNR↑	SSIM↑	LPIPS↓	PSNR↑	SSIM↑	LPIPS↓	PSNR↑	SSIM↑	LPIPS↓	PSNR↑	SSIM↑	LPIPS↓	PSNR↑	SSIM↑	LPIPS↓	PSNR↑	SSIM↑	LPIPS↓
<b>FBP</b>	18.30	0.573	0.2452	14.19	0.463	0.3038	8.26	0.275	0.4519	16.22	0.316	0.1914	13.92	0.255	0.2771	11.34	0.178	0.3688
<b>TV [57]</b>	27.64	0.841	0.1101	23.32	0.758	0.1536	20.52	0.692	0.1967	23.37	0.489	0.2959	21.37	0.379	0.3380	19.48	0.330	0.3775
<b>NafNet [49]</b>	<b>44.31</b>	<b>0.985</b>	0.0320	<b>41.09</b>	<b>0.975</b>	0.0525	<b>36.35</b>	<b>0.957</b>	0.0684	<b>37.57</b>	<b>0.971</b>	0.0518	<b>33.68</b>	<b>0.949</b>	0.0776	<b>30.29</b>	<b>0.918</b>	0.1037
<b>DPS [39]</b>	38.76	0.951	<b>0.0123</b>	30.10	0.850	0.0414	26.48	0.849	<b>0.0370</b>	29.78	0.858	0.0642	25.39	0.820	0.0954	21.60	0.764	0.1415
<b>DDNM+ [37]</b>	35.39	0.907	0.0145	31.69	0.859	<b>0.0348</b>	27.18	0.813	0.0449	21.31	0.655	0.2087	20.26	0.637	0.2344	18.29	0.601	0.2939
<b>DOLCE [42]</b>	42.61	0.978	<b>0.0119</b>	38.47	0.959	<b>0.0140</b>	31.36	0.915	<b>0.0280</b>	35.80	0.956	<b>0.0180</b>	32.41	0.928	<b>0.0325</b>	28.57	0.879	<b>0.0479</b>
<b>RN-SDE</b>	<b>43.94</b>	<b>0.982</b>	0.0069	<b>40.43</b>	<b>0.965</b>	0.0086	<b>35.62</b>	<b>0.939</b>	0.0143	<b>36.86</b>	<b>0.960</b>	<b>0.0257</b>	<b>32.89</b>	<b>0.936</b>	<b>0.0393</b>	<b>29.53</b>	<b>0.902</b>	<b>0.0629</b>
<b>RN-SDE SA</b>	<b>45.36</b>	<b>0.987</b>	0.0238	<b>41.92</b>	<b>0.976</b>	0.0390	<b>36.55</b>	<b>0.954</b>	0.0539	<b>37.38</b>	<b>0.966</b>	<b>0.0464</b>	<b>33.61</b>	<b>0.948</b>	<b>0.0713</b>	<b>30.00</b>	<b>0.915</b>	<b>0.0980</b>

Note: The best, second-best and the third-best values for each metric have been highlighted with colors.

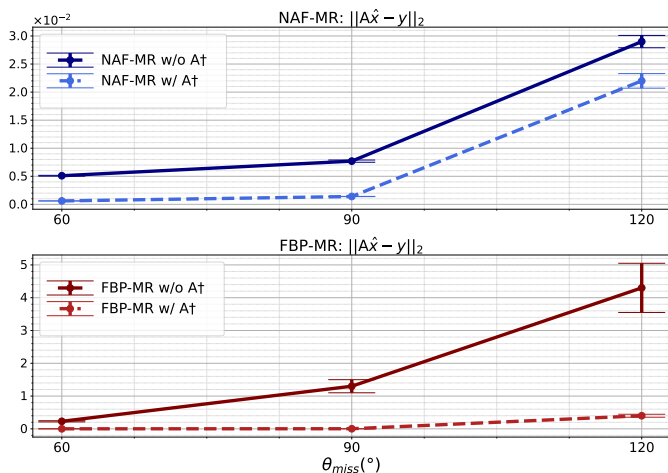


Fig. 7. Visualization of the data consistency error:  $\|\mathbf{A}\hat{\mathbf{x}} - \mathbf{y}\|_2$ . Compared to **FBP-MR**, **NAF-MR** shows a smaller consistency error, but this gap narrows after the introduction of RNSD rectification. Notably, including RNSD-based rectification significantly enhances and stabilizes reconstruction performance, as evidenced by a considerable reduction in the mean and standard deviation.

search over the data consistency parameters for DPS, DDNM+, and DOLCE and adopt the same DDPM diffusion setting. For the C4KC-KiTS dataset, we directly copy the diffusion setting provided in DOLCE to train both conditional and unconditional DDPM diffusion models. We also perform a grid search over the data consistency parameters for DPS and DDNM+. Importantly, we train different models for different LACT scenarios and always use the standard DDPM sampling scheme without skipping.

As expected, in terms of perceptual quality, as indicated by the LPIPS metric, all diffusion-based reconstruction methods achieve satisfactory results. Among them, RN-SDE and DOLCE stand out, significantly outperforming others, with each showing competitive performance across the two datasets, and the differences between them are negligible. Furthermore, in terms of PSNR and SSIM, RN-SDE beats DOLCE across all experimental cases on both datasets. For NafNet and RN-SDE, as previously mentioned, a direct comparison between these two experiments is not entirely fair. Nevertheless, the difference between RN-SDE and

NafNet remains minimal. Nevertheless, the gap between RN-SDE and NafNet remains small. In fact, concerning PSNR and SSIM, the difference between RN-SDE and NafNet across all experimental settings stays within 1 dB for PSNR and 0.02 for SSIM. However, in terms of perceptual quality, RN-SDE outperforms NafNet by several times. When comparing RN-SDE SA to NafNet, RN-SDE SA achieves a clear advantage on the ChromSTEM dataset, while for the C4KC-KiTS dataset, this gap narrows to 0.3 dB for PSNR and 0.005 for SSIM.

**Model Complexity and Runtime Efficiency.** In Table IV, we compared the computational complexity of the sampling process in four diffusion-based models across four aspects: FLOPs, number of parameters, and time consumption, using both the ChromSTEM and C4KC-KiTS datasets. We reported the total time consumption for the sampling process, along with the corresponding number of iterations required. The iterations for RN-SDE include Time-Travel, which can be measured by Eq. 20. In the ChromSTEM dataset, we set the travel length to  $l = 4$  and the travel repetition to  $r = 2$ , while for the C4KC dataset, we adjusted the travel length to  $l = 8$ . All experiments were conducted using a single Nvidia Quadro RTX 8000 GPU and an Intel Xeon Gold 6226R CPU with a batch size of 1. In DOLCE, we used our own implementation of the Radon forward/backward transform, which may lead to differences in execution efficiency. Therefore, we must emphasize that the provided **time are approximate and intended for reference only.**

The table highlights that RN-SDE offers a clear advantage over DOLCE in terms of both computational complexity and runtime efficiency. Specifically, RN-SDE requires significantly fewer FLOPs and parameters, completing the sampling process in a fraction of the time compared to DOLCE, which exhibits the highest time consumption on both datasets. Notably, RN-SDE achieves these improvements while also outperforming DOLCE in key performance metrics such as PSNR, SSIM, and LPIPS, making it a more efficient and effective choice overall.

**Visual Evaluation.** We compare several representative visual results of our proposed RN-SDE with those from NafNet,

TABLE IV

COMPARISON OF MODEL COMPLEXITY AND RUNTIME EFFICIENCY. EXPERIMENTS ARE BASED ON A SINGLE NVIDIA QUADRO RTX 8000 GPU, AND AN INTEL(R) XEON(R) GOLD 6226R CPU

Method	Backbone	#GMacs	#Params	Time	Iters
<i>ChromSTEM Dataset</i>					
DPS	UNet	4.94e+4	93.61 M	171s	1000
DDNM+	UNet	4.93e+4	93.61 M	126s	1000
DOLCE	CondUNet	5.34e+4	93.63 M	4634s	1000
RN-SDE	CondNafNet	6.02e+3	70.08 M	66s	593
<i>CAKC-KiTS Dataset</i>					
DPS	UNet	7.20e+5	94.53 M	951s	2000
DDNM+	UNet	7.18e+5	94.53 M	1011s	2000
DOLCE	CondUNet	8.39e+5	94.53 M	10875s	2000
RN-SDE	CondNafNet	9.92e+4	85.72 M	106s	585

Note: Different implementations may result in variations in code execution efficiency, the times presented are approximate and intended for reference only.

DPS, and DOLCE. As shown in Fig. 6 and Fig. 5, several notable characteristics can be observed: for both datasets, while the NafNet reconstructions perform well in terms of PSNR and SSIM metrics, the visual results show a clear lack of high-frequency details, leading to visible blurring, particularly in cases with 120° angle missing. In contrast, the visual results of the other three diffusion models all exhibit satisfactory perceptual quality, which can be attributed to the nature of diffusion models that directly model the entire image distribution and sample from the posterior. Among them, DPS shows weaker data consistency compared to DOLCE and RN-SDE. We hypothesize that this disparity is partially due to DPS not using low-quality reconstructions as a condition to guide the diffusion process. As for DOLCE and RN-SDE, their visual results show no significant differences. As mentioned earlier, the primary difference between these models lies in their complexity and the time consumption during the sampling process, which will not be elaborated further here.

## V. CONCLUSION & DISCUSSION

In this paper, we address the problem of LACT reconstruction under noise-free conditions. Building upon diffusion stochastic differential equations, we introduce RN-SDEs, a novel NafNet-based diffusion framework that leverages pre-trained mean-reverting SDEs as image priors for high-quality CT reconstruction. Specifically, we use FBP reconstructions as the *mean* to initialize and condition the reverse diffusion process, which has been proven to remarkably reduce the diffusion time steps required for convergence and achieve better perceptual quality. To further enforce data consistency, we incorporate an additional rectification step based on RNSD during each iteration, which involves replacing the range-space contents of the intermediate clean estimation while preserving the null-space contents intact. Crucially, the Radon pseudo-inverse used in this process is estimated by a separate neural network with a combined objective. We demonstrate the

effectiveness and generalizability of RN-SDEs through comprehensive experiments on several LACT scenarios based on two different datasets with distinct data distributions. In summary, RN-SDEs offer a robust and efficient solution for LACT reconstruction, achieving SOTA performance while maintaining computational efficiency. This work paves the way for future research to apply diffusion-based methods to solve various IR tasks and explore their applications in broader imaging contexts.

## VI. REFERENCES SECTION

### REFERENCES

- [1] S. Liu, S. Liu, C. Ji, H. Zheng, X. Pan, Y. Zhang, W. Guan, L. Chen, Y. Guan, W. Li *et al.*, "Application of ct texture analysis in predicting histopathological characteristics of gastric cancers," *European radiology*, vol. 27, pp. 4951–4959, 2017.
- [2] L. De Chiffre, S. Carmignato, J.-P. Kruth, R. Schmitt, and A. Weckenmann, "Industrial applications of computed tomography," *CIRP annals*, vol. 63, no. 2, pp. 655–677, 2014.
- [3] I. Domingues, G. Pereira, P. Martins, H. Duarte, J. Santos, and P. H. Abreu, "Using deep learning techniques in medical imaging: a systematic review of applications on ct and pet," *Artificial Intelligence Review*, vol. 53, pp. 4093–4160, 2020.
- [4] K. A. Miles, C. Charnsangavej, F. T. Lee, E. K. Fishman, K. Horton, and T.-Y. Lee, "Application of ct in the investigation of angiogenesis in oncology," *Academic radiology*, vol. 7, no. 10, pp. 840–850, 2000.
- [5] J. Radon, "U ber die bestimmung von funktionen durch ihre integralwerte langs gewisser mannigfaltigkeiten; ber. vor sachs.," *Akad. Wiss*, vol. 69, p. 262, 1917.
- [6] D. E. Dudgeon, "Multidimensional digital signal processing," *Engewood Cliffs*, 1983.
- [7] R. N. Bracewell, "Strip integration in radio astronomy," *Australian Journal of Physics*, vol. 9, no. 2, pp. 198–217, 1956.
- [8] G. S. Alberti, E. De Vito, M. Lassas, L. Ratti, and M. Santacesaria, "Learning the optimal tikhonov regularizer for inverse problems," *Advances in Neural Information Processing Systems*, vol. 34, pp. 25 205–25 216, 2021.
- [9] S. Barutcu, S. Aslan, A. K. Katsaggelos, and D. Gürsoy, "Limited-angle computed tomography with deep image and physics priors," *Scientific reports*, vol. 11, no. 1, p. 17740, 2021.
- [10] A. Danielyan, V. Katkovich, and K. Egiazarian, "Bm3d frames and variational image deblurring," *IEEE Transactions on image processing*, vol. 21, no. 4, pp. 1715–1728, 2011.
- [11] H. Kudo, T. Suzuki, and E. A. Rashed, "Image reconstruction for sparse-view ct and interior ct—introduction to compressed sensing and differentiated backprojection," *Quantitative imaging in medicine and surgery*, vol. 3, no. 3, p. 147, 2013.
- [12] R. Anirudh, H. Kim, J. J. Thiagarajan, K. A. Mohan, K. Champley, and T. Bremer, "Lose the views: Limited angle ct reconstruction via implicit sinogram completion," in *Proceedings of the IEEE Conference on Computer Vision and Pattern Recognition*, 2018, pp. 6343–6352.
- [13] H. Gupta, K. H. Jin, H. Q. Nguyen, M. T. McCann, and M. Unser, "Cnn-based projected gradient descent for consistent ct image reconstruction," *IEEE transactions on medical imaging*, vol. 37, no. 6, pp. 1440–1453, 2018.
- [14] Y. Han and J. C. Ye, "Framing u-net via deep convolutional framelets: Application to sparse-view ct," *IEEE transactions on medical imaging*, vol. 37, no. 6, pp. 1418–1429, 2018.
- [15] K. H. Jin, M. T. McCann, E. Froustey, and M. Unser, "Deep convolutional neural network for inverse problems in imaging," *IEEE transactions on image processing*, vol. 26, no. 9, pp. 4509–4522, 2017.
- [16] Q. Zhang, Z. Hu, C. Jiang, H. Zheng, Y. Ge, and D. Liang, "Artifact removal using a hybrid-domain convolutional neural network for limited-angle computed tomography imaging," *Physics in Medicine & Biology*, vol. 65, no. 15, p. 155010, 2020.
- [17] Y. Zhang, T. Lv, R. Ge, Q. Zhao, D. Hu, L. Zhang, J. Liu, Y. Zhang, Q. Liu, W. Zhao *et al.*, "Cd-net: Comprehensive domain network with spectral complementary for dect sparse-view reconstruction," *IEEE Transactions on Computational Imaging*, vol. 7, pp. 436–447, 2021.



- [18] B. Kawar, G. Vaksman, and M. Elad, “Snips: Solving noisy inverse problems stochastically,” *Advances in Neural Information Processing Systems*, vol. 34, pp. 21 757–21 769, 2021.
- [19] I. Goodfellow, J. Pouget-Abadie, M. Mirza, B. Xu, D. Warde-Farley, S. Ozair, A. Courville, and Y. Bengio, “Generative adversarial nets,” *Advances in neural information processing systems*, vol. 27, 2014.
- [20] D. P. Kingma and M. Welling, “Auto-encoding variational bayes,” *arXiv preprint arXiv:1312.6114*, 2013.
- [21] J. Ho, A. Jain, and P. Abbeel, “Denoising diffusion probabilistic models,” *Advances in neural information processing systems*, vol. 33, pp. 6840–6851, 2020.
- [22] A. Van Den Oord, O. Vinyals *et al.*, “Neural discrete representation learning,” *Advances in neural information processing systems*, vol. 30, 2017.
- [23] T. Karras, S. Laine, and T. Aila, “A style-based generator architecture for generative adversarial networks,” in *Proceedings of the IEEE/CVF conference on computer vision and pattern recognition*, 2019, pp. 4401–4410.
- [24] Y. Song and S. Ermon, “Generative modeling by estimating gradients of the data distribution,” *Advances in neural information processing systems*, vol. 32, 2019.
- [25] Y. Song, J. Sohl-Dickstein, D. P. Kingma, A. Kumar, S. Ermon, and B. Poole, “Score-based generative modeling through stochastic differential equations,” *arXiv preprint arXiv:2011.13456*, 2020.
- [26] N. Heller, N. Sathianathan, A. Kalapara, E. Walczak, K. Moore, H. Kaluzniak, J. Rosenberg, P. Blake, Z. Rengel, M. Oestreich *et al.*, “The kits19 challenge data: 300 kidney tumor cases with clinical context, ct semantic segmentations, and surgical outcomes,” *arXiv preprint arXiv:1904.00445*, 2019.
- [27] R. Zhang, P. Isola, A. A. Efros, E. Shechtman, and O. Wang, “The unreasonable effectiveness of deep features as a perceptual metric,” in *Proceedings of the IEEE conference on computer vision and pattern recognition*, 2018, pp. 586–595.
- [28] P. Dhariwal and A. Nichol, “Diffusion models beat gans on image synthesis,” *Advances in neural information processing systems*, vol. 34, pp. 8780–8794, 2021.
- [29] F.-A. Croitoru, V. Hondru, R. T. Ionescu, and M. Shah, “Diffusion models in vision: A survey,” *IEEE Transactions on Pattern Analysis and Machine Intelligence*, 2023.
- [30] L. Yang, Z. Zhang, Y. Song, S. Hong, R. Xu, Y. Zhao, W. Zhang, B. Cui, and M.-H. Yang, “Diffusion models: A comprehensive survey of methods and applications,” *ACM Computing Surveys*, vol. 56, no. 4, pp. 1–39, 2023.
- [31] A. Q. Nichol and P. Dhariwal, “Improved denoising diffusion probabilistic models,” in *International conference on machine learning*. PMLR, 2021, pp. 8162–8171.
- [32] J. Sohl-Dickstein, E. Weiss, N. Maheswaranathan, and S. Ganguli, “Deep unsupervised learning using nonequilibrium thermodynamics,” in *International conference on machine learning*. PMLR, 2015, pp. 2256–2265.
- [33] Y. Song and S. Ermon, “Improved techniques for training score-based generative models,” *Advances in neural information processing systems*, vol. 33, pp. 12 438–12 448, 2020.
- [34] Y. Song, C. Durkan, I. Murray, and S. Ermon, “Maximum likelihood training of score-based diffusion models,” *Advances in neural information processing systems*, vol. 34, pp. 1415–1428, 2021.
- [35] Q. Liu, J. Lee, and M. Jordan, “A kernelized stein discrepancy for goodness-of-fit tests,” in *International conference on machine learning*. PMLR, 2016, pp. 276–284.
- [36] K. Chwialkowski, H. Strathmann, and A. Gretton, “A kernel test of goodness of fit,” in *International conference on machine learning*. PMLR, 2016, pp. 2606–2615.
- [37] Y. Wang, J. Yu, and J. Zhang, “Zero-shot image restoration using denoising diffusion null-space model,” in *The Eleventh International Conference on Learning Representations*, 2023.
- [38] J. Choi, S. Kim, Y. Jeong, Y. Gwon, and S. Yoon, “Ilvr: Conditioning method for denoising diffusion probabilistic models,” *arXiv preprint arXiv:2108.02938*, 2021.
- [39] H. Chung, J. Kim, M. T. Mccann, M. L. Klasky, and J. C. Ye, “Diffusion posterior sampling for general noisy inverse problems,” in *The Eleventh International Conference on Learning Representations, ICLR 2023*. The International Conference on Learning Representations, 2023.
- [40] H. Chung, B. Sim, D. Ryu, and J. C. Ye, “Improving diffusion models for inverse problems using manifold constraints,” *Advances in Neural Information Processing Systems*, vol. 35, pp. 25 683–25 696, 2022.
- [41] Y. Song, L. Shen, L. Xing, and S. Ermon, “Solving inverse problems in medical imaging with score-based generative models,” *arXiv preprint arXiv:2111.08005*, 2021.
- [42] J. Liu, R. Anirudh, J. J. Thiagarajan, S. He, K. A. Mohan, U. S. Kamilov, and H. Kim, “Dolce: A model-based probabilistic diffusion framework for limited-angle ct reconstruction,” in *Proceedings of the IEEE/CVF International Conference on Computer Vision*, 2023, pp. 10 498–10 508.
- [43] Z. Luo, F. K. Gustafsson, Z. Zhao, J. Sjölund, and T. B. Schön, “Image restoration with mean-reverting stochastic differential equations,” *arXiv preprint arXiv:2301.11699*, 2023.
- [44] Y. Blau and T. Michaeli, “The perception-distortion tradeoff,” in *Proceedings of the IEEE conference on computer vision and pattern recognition*, 2018, pp. 6228–6237.
- [45] C. Saharia, J. Ho, W. Chan, T. Salimans, D. J. Fleet, and M. Norouzi, “Image super-resolution via iterative refinement,” *IEEE transactions on pattern analysis and machine intelligence*, vol. 45, no. 4, pp. 4713–4726, 2022.
- [46] H. Li, Y. Yang, M. Chang, S. Chen, H. Feng, Z. Xu, Q. Li, and Y. Chen, “Srdiff: Single image super-resolution with diffusion probabilistic models,” *Neurocomputing*, vol. 479, pp. 47–59, 2022.
- [47] J. Schwab, S. Antholzer, and M. Haltmeier, “Deep null space learning for inverse problems: convergence analysis and rates,” *Inverse Problems*, vol. 35, no. 2, p. 025008, 2019.
- [48] R. Penrose, “A generalized inverse for matrices,” in *Mathematical proceedings of the Cambridge philosophical society*, vol. 51. Cambridge University Press, 1955, pp. 406–413.
- [49] L. Chen, X. Chu, X. Zhang, and J. Sun, “Simple baselines for image restoration,” in *European conference on computer vision*. Springer, 2022, pp. 17–33.
- [50] R. J. Elliott and B. D. Anderson, “Reverse time diffusions,” *Stochastic processes and their applications*, vol. 19, no. 2, pp. 327–339, 1985.
- [51] A. Hyvärinen and P. Dayan, “Estimation of non-normalized statistical models by score matching,” *Journal of Machine Learning Research*, vol. 6, no. 4, 2005.
- [52] P. Vincent, “A connection between score matching and denoising autoencoders,” *Neural computation*, vol. 23, no. 7, pp. 1661–1674, 2011.
- [53] Y. Song, S. Garg, J. Shi, and S. Ermon, “Sliced score matching: A scalable approach to density and score estimation,” in *Uncertainty in Artificial Intelligence*. PMLR, 2020, pp. 574–584.
- [54] Z. Luo, F. K. Gustafsson, Z. Zhao, J. Sjölund, and T. B. Schön, “Refusion: Enabling large-size realistic image restoration with latent-space diffusion models,” in *Proceedings of the IEEE/CVF Conference on Computer Vision and Pattern Recognition Workshops*, 2023, pp. 1680–1691.
- [55] M. Carignano, M. Kröger, L. Almassalha, V. Agrawal, W. S. Li, E. M. Pujadas, R. J. Nap, V. Backman, and I. Szleifer, “Local volume concentration, packing domains and scaling properties of chromatin,” *Research Square*, 2023.
- [56] N. Heller, F. Isensee, K. H. Maier-Hein, X. Hou, C. Xie, F. Li, Y. Nan, G. Mu, Z. Lin, M. Han *et al.*, “The state of the art in kidney and kidney tumor segmentation in contrast-enhanced ct imaging: Results of the kits19 challenge,” *Medical image analysis*, vol. 67, p. 101821, 2021.
- [57] A. Chambolle and T. Pock, “A first-order primal-dual algorithm for convex problems with applications to imaging,” *Journal of mathematical imaging and vision*, vol. 40, pp. 120–145, 2011.
- [58] D. Gürsoy, F. De Carlo, X. Xiao, and C. Jacobsen, “Tomopy: a framework for the analysis of synchrotron tomographic data,” *Journal of synchrotron radiation*, vol. 21, no. 5, pp. 1188–1193, 2014.
- [59] J. Whang, M. Delbraccio, H. Talebi, C. Saharia, A. G. Dimakis, and P. Milanfar, “Deblurring via stochastic refinement,” in *Proceedings of the IEEE/CVF Conference on Computer Vision and Pattern Recognition*, 2022, pp. 16 293–16 303.

## APPENDIX

### A. Generalize DDPMs and SGMs to SDEs

Recall the one-step DDPM [21] forward diffusion process, which gradually transforms the data distribution  $q(\mathbf{x}_0)$  into noise.

$$\mathbf{x}_t = \sqrt{1 - \beta_t} \mathbf{x}_{t-1} + \sqrt{\beta_t} \mathcal{N}(0, \mathbf{I}), \quad \forall t \in \{1, \dots, T\}$$



In SDEs, the diffusion process is considered to be continuous, thus becoming the solution of an SDE. In other words, we will take infinite steps and each step will be infinitely small.

$$\begin{aligned}\mathbf{x}_t &= \sqrt{1 - \beta_t} \mathbf{x}_{t-1} + \sqrt{\beta_t} \mathcal{N}(\mathbf{0}, \mathbf{I}) \\ &\approx \mathbf{x}_{t-1} - \frac{\beta(t)\Delta t}{2} \mathbf{x}_{t-1} + \sqrt{\beta(t)\Delta t} \mathcal{N}(\mathbf{0}, \mathbf{I})\end{aligned}$$

Note that the last approximation is obtained using Taylor Expansion. Therefore, this iterative update will correspond to a certain solution or a certain discretization of an SDE:

$$d\mathbf{x} = \underbrace{-\frac{1}{2}\beta(t)\mathbf{x} dt}_{\text{drift term}} + \underbrace{\sqrt{\beta(t)}d\mathbf{w}}_{\text{diffusion term}}$$

Similarly, people can also easily start from the one-step SGM [24] forward diffusion process:

$$\mathbf{x}_t = \mathbf{x}_{t-1} + \sqrt{\sigma_t^2 - \sigma_{t-1}^2} \mathcal{N}(0, \mathbf{I}), \quad \forall t \in \{1, \dots, T\}$$

to its corresponding SDE version:

$$d\mathbf{x} = \sqrt{\frac{d[\sigma(t)^2]}{dt}} d\mathbf{w},$$

### B. RNSD With Maximum Likelihood Objective

The training process in this paper follows a manner similar to conventional score matching. However, the objective differs as it aims to identify an  $\mathbf{x}_{t-1}$  that maximizes the log-likelihood,  $\log p(\mathbf{x}_{t-1} | \mathbf{x}_t, \hat{\mathbf{x}}_0)$ . A theoretical optimal solution,  $\mathbf{x}_{i-1}^*$ , is provided by [43] as follows:

$$\begin{aligned}\mathbf{x}_{t-1}^* &= \frac{1 - e^{-2\bar{\theta}_{t-1}}}{1 - e^{-2\bar{\theta}_t}} e^{-\theta'_t} (\mathbf{x}_t - \mu) \\ &\quad + \frac{1 - e^{-2\theta'_t}}{1 - e^{-2\bar{\theta}_t}} e^{-\bar{\theta}_{t-1}} (\mathbf{x}_0 - \mu) + \mu.\end{aligned}$$

Building on this foundation, recall the reverse MR-SDE described in Eq. 19, which allows us to sample the next state,  $\mathbf{x}_{t-1}$ , by leveraging only the score,  $\nabla_{\mathbf{x}} \log p(\mathbf{x}_t | \mathbf{x}_0)$ , and the previous state,  $\mathbf{x}_t$ . To ensure that the reverse diffusion adheres to the optimal trajectory, the training is designed to minimize the  $l_2$  distance between the theoretically derived  $\mathbf{x}_{t-1}^*$  and the practical transition,  $\mathbf{x}_t - (d\mathbf{x})_{\tilde{s}_\phi}$ . Upon convergence, the model is expected to exhibit the following relationship:

$$\begin{aligned}\mathbf{x}_{t-1}^* &= \mathbf{x}_t - \left[ \theta_t (\mu - \mathbf{x}_t) \right. \\ &\quad \left. - \sigma_t^2 \tilde{s}_\phi(\mathbf{x}_t, \mu, t) \right] dt \\ &\quad + \sigma_t d\hat{\mathbf{w}},\end{aligned}$$

where  $s_\phi(\mathbf{x}_t, \mu, t)$  is the learned score function. Bringing  $\mathbf{x}_{i-1}^*$  into the above equation and simplifying, we arrive at two important derivations, the first of which corresponds to Eq. 15, which says that the objective of maximum likelihood is equivalent to estimate the optimal score,  $\nabla_{\mathbf{x}} \log p(\mathbf{x}_t | \mathbf{x}_0)^*$ :

$$\nabla_{\mathbf{x}} \log p(\mathbf{x}_t | \mathbf{x}_0)^* = \frac{\mathbf{G}_t \mathbf{x}_t + \mathbf{H}_t \mathbf{x}_0 - (\mathbf{H}_t + \mathbf{G}_t) \mu}{\sigma_t^2 dt}$$

Here, let  $\theta'_t := \int_{t-1}^t \theta_z dz$ , the coefficient  $\mathbf{G}_t, \mathbf{H}_t$  are respectively:

$$\begin{aligned}\mathbf{G}_t &= \frac{1 - e^{-2\bar{\theta}_{t-1}}}{1 - e^{-2\bar{\theta}_t}} e^{-\theta'_t} - \theta'_t - 1 \\ \mathbf{H}_t &= \frac{1 - e^{-2\theta'_t}}{1 - e^{-2\bar{\theta}_t}} e^{-\bar{\theta}_{t-1}}\end{aligned}$$

Based on this, we can obtain the training objective, given by:

$$\mathbb{E}_{t \in \mathcal{U}} \mathbb{E}_{p(\mathbf{x}_t)} [\| \nabla_{\mathbf{x}} \log p(\mathbf{x}_t | \mathbf{x}_0)^* - \tilde{s}_\phi(\mathbf{x}_t, \mu, t) \|],$$

where the reverse diffusion model  $\tilde{s}_\phi(\mathbf{x}_t, \mu, t)$  is a Conditional NafNet [54], which we provide the details in Appx. D.

Another useful derivation is that we can extract  $x_0 \mathbf{x}_0$  from the equation as a clean estimation of  $x_0 \mathbf{x}_0$  at the time  $tt$ . For the sake of clarity, we denote it as  $x_0 | t \mathbf{x}_{0|t}$ , measured by the equation (Eq. 17) below:

$$\mathbf{x}_{0|t} = -\frac{\mathbf{G}_t}{\mathbf{H}_t} \mathbf{x}_t + \frac{\sigma_t^2}{\mathbf{H}_t} s_\phi(\mathbf{x}_t, \mu, t) dt + (1 + \frac{\mathbf{G}_t}{\mathbf{H}_t}) \mu.$$

We will utilize the rectified intermediate state,  $\hat{\mathbf{x}}_{0|t}$ , to update the score in Eq. 15 (by replacing  $\mathbf{x}_0$  with  $\hat{\mathbf{x}}_{0|t}$ ). The revised score,  $\nabla_{\mathbf{x}} \log p(\mathbf{x}_t | \hat{\mathbf{x}}_{0|t})^*$ , is subsequently integrated into the reverse MR-SDE to complete a refinement iteration. The entire process is encapsulated in the following equation:

$$\begin{aligned}\mathbf{x}_{t-1} &= \mathbf{H}_t \hat{\mathbf{x}}_{0|t} + (\mathbf{G}_t + \theta_t dt) \mathbf{x}_t \\ &\quad - (\mathbf{H}_t + \mathbf{G}_t + \theta_t dt) \mu + \sigma_t \sqrt{dt} \epsilon_t, \quad \epsilon_t \sim \mathcal{N}(0, \mathbf{I})\end{aligned}$$

By replacing  $\mathbf{x}_t - \mathbf{x}_{t-1}$  with  $d\mathbf{x}$  and rearranging, the above formulation can be transformed into the following reverse RN-SDE:

$$d\mathbf{x} = (\mathbf{G}_t + \theta_t dt)(\mu - \mathbf{x}_t) + \mathbf{H}_t(\mu - \mathbf{x}_{0|t}) + \sigma_t d\hat{\mathbf{w}},$$

### C. Implementation of Learnable Radon Back-Projection

For any arbitrary 2D object  $f(x, y)$ , we consider the tomographic measurement process at a given angle  $\theta$  to consist of a set of line integrals and the sinogram is the collection of such scans over a set of angles. Therefore, the value of any position  $r$  in the image, where the point  $(x, y)$  will be projected at angle  $\theta$  can be measured by:

$$x \cos \theta + y \sin \theta = r \quad (24)$$

and the corresponding Radon transform can be written as:

$$p_\theta(r) = \int_{-\infty}^{\infty} \int_{-\infty}^{\infty} f(x, y) \delta(x \cos \theta + y \sin \theta - r) dx dy \quad (25)$$

where  $\delta(\cdot)$  denotes the Dirac functions and  $p_\theta(r)$  represents the radon projection of  $f(x, y)$ , which is the input for the Learnable Radon Back-Projection. To reverse this process and reconstruct  $f(x, y)$ , similar to FBP, we use a learnable Ramp filter to filter  $p_\theta(r)$ . This filtering is typically performed by transforming the frequency response of the Ramp filter,  $|\omega|$ , which can be modeled as a simple MLP. When the transformation is the identity function, the learnable back-projection becomes equivalent to standard FBP (recommended for some simple cases). For simplicity, we denote the learnable Ramp filter as  $\omega_\eta$ . The filtered sinogram,  $q_\theta(r)$ , can be expressed as:

$$q_\theta(r) = \mathcal{F}^{-1} \{ |\omega_\eta| \cdot \mathcal{F} \{ p_\theta(r) \} \}; \quad (26)$$

and can be transformed back to the image domain through:

$$f(x, y) = \int_0^\pi q_\theta(r) d\theta \quad (27)$$

where  $d\theta$  is the angular spacing between the projections.

#### D. Cond-NafNet With Time Embedding

NafNet, proposed by Chen et al. [49], represents a simple yet efficient framework for image restoration that has achieved state-of-the-art results across various tasks. While retaining the foundational U-Net architecture, NafNet replaces traditional nonlinear activation functions with linear operations such as multiplication, enhancing its performance and effectiveness.

To adapt NafNet for diffusion applications, [54] have implemented several enhancements to the original framework described by [49] and named it Conditional NafNet. Figure 8 shows the structure of a basic NafBlock within the Conditional NafNet, with the primary modification being an additional embedding input designed to encode the timestep information of the diffusion process. This timestep information is processed through a designated *Emb layer* and subsequently integrated with the image signal via scale-shift normalization. It is worth emphasizing that the timestep information must be encoded into both the In and Out layers; otherwise, the model will fail to learn accurate time information, leading to improper convergence of the diffusion process. Moreover, dropout is introduced to both *In/Out Layer* to prevent overfitting during training.

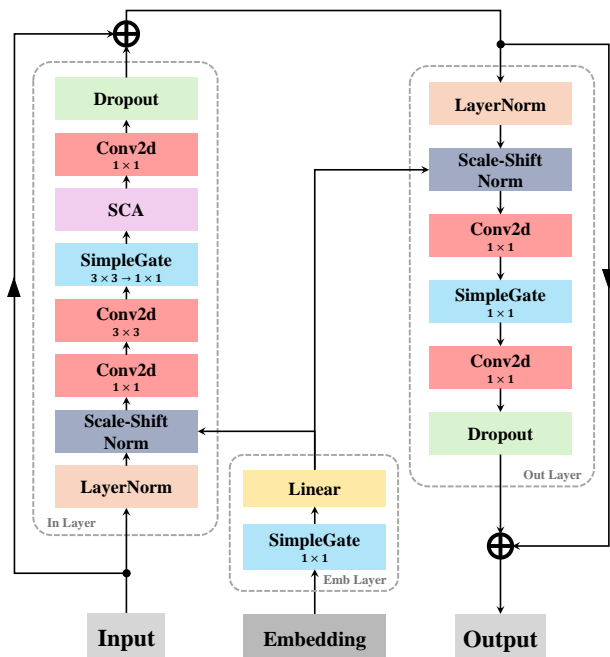


Fig. 8. Structure of a single NafBlock within Cond-NafNet, adapted specifically for diffusion processes. Key modifications include an *Emb layer* for processing additional embedding information and *dropout* layers in both *In/Out Layer* to prevent overfitting.